Journal of
Materials Chemistry C

Materials for optical, magnetic and electronic devices

Accepted Manuscript

This article can be cited before page numbers have been issued, to do this please use: H. Spieser, Z. Tehrani, M. Ali, E. Daghigh Ahmadi, A. Denneulin, J. Bras, D. Deganello and D. T. Gethin, *J. Mater. Chem. C*, 2021, DOI: 10.1039/D0TC04553E.

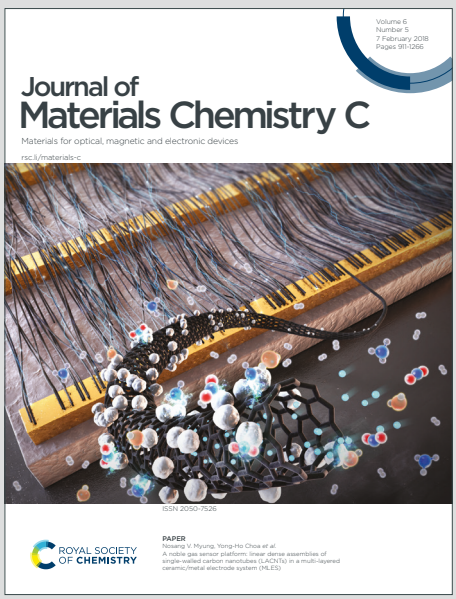

ROYAL SOCIETY OF CHEMISTRY

rsc.li/materials-c

View Article Online
DOI: 10.1039/D0TC04553E

ARTICLE

Metal Organic Framework sensors on flexible substrate for ammonia sensing application at room temperature

Received 00th January 20xx,
Accepted 00th January 20xx

DOI: 10.1039/x0xx00000x

Hugo Spieser[a, b], Zari Tehrani*[b, c], Muhammad Ali[c], Ehsaneh Daghigh Ahmadi[c], Aurore Denneulin[a], Julien Bras[a,d], Davide Deganello[b], David Gethin[b]

The application of sensitive gas sensors manufactured in high volume at low cost has great interest due to an extensive array of potential applications. Such areas include industrial processing, biotechnology and intelligent food packaging. This work reports a straightforward and versatile technique using screen-printing and drop-casting processes, to produce gas sensors on a flexible plastic substrate, based on a combination of metal organic framework and graphene-carbon materials. We demonstrate a sensitive and stable ammonia sensor (4.6% maximal response) over a range from 20 to 100 ppm. The optimized formulation is 36 times higher than a carbon-graphene only sensor and makes the developed devices suitable for intelligent packaging. The sensors production process is fast, reliable and low-cost and so there is a strong potential for the process principles to be adapted industrially for a different gas target or application.

1. Introduction

The capability to adsorb, separate or sense gas molecules in our environment remain nowadays a great challenge in several fields of applications to tackle social issues such as greenhouse gas emission or human health and safety. Different 3D porous materials have been investigated for gas sensor applications, including Metal Organic Frameworks (MOFs). MOFs are crystalline and microporous materials based on the coordination of metallic centres with organic ligands[1]. They display very large surface areas, high porosity and offer almost infinite possibilities in terms of designing and building architecture[2].

Electrical gas sensors based on MOFs technology are mainly prepared either using in-situ growing of MOF crystals onto electrodes[3,4], by preparing pressed pellets[5–7] or by coating a MOF slurry onto electrodes with different processes such as spin-coating, drop-casting, or even screen printing[8–10]. However, despite MOFs promising gas adsorption properties, a lot of application in electronics are still challenging due to their poor conductivity[11]. Indeed, MOFs are mainly described as insulators and their conductivity is usually lower than 10^{-10} S.cm^{-1} as they do not present any low energy charge transport pathway. To solve this issue, MOFs can be mixed and used along with conducting nano- or micro-materials and especially conductive carbon materials as shown recently[12].

Up to now, the reported sensing target gases for such MOFs/micro- and nano-carbon composites are different volatile organic compounds (VOCs), hydrogen, or ammonia. Fardindoost et al. (2017) researched a combination of graphene oxide and cobalt-base MOF produced by in-situ synthesis for promising selective hydrogen sensing[13]. Different VOC sensing was conducted recently by Jafari et al. (2019) using Zeolitic Imidazolate Framework-8 (ZIF-8) and ZIF-67 MOF with carbon nanotubes and silver nanoparticles[14]. Several examples also reported the use of MOF-derived oxides along with nano-carbon materials for acetone, ethanol or sulphur dioxide sensing[15–18]. The different MOF derived-oxides tested showed sensitive, selective, fast, and stable sensing characteristics.

Ammonia is an industrial by-product and is a toxic gas even at very low concentration and thus there is a need for efficient ammonia sensors. The detection of ammonia and other volatile amines is also of interest for smart packaging applications as they are known to be indicators of spoilage of fresh fish and seafood[19,20]. Travlou et al. (2015) was the first group to report resistance change ammonia sensing featuring a combination of graphene derivatives and MOF[21]. Copper benzene-1,3,5-tricarboxylate (abbreviated CuBTC or HKUST-1 with BTC being 1,3,5-benzenetricarboxylate ligand) MOF was synthesized in-situ with aminated-graphite oxide, processed into the slurry in Dimethylformamide (DMF) and blade-spread on gold interdigitated electrodes (IDE). The prepared sensors were working at room temperature, with a 100-500 ppm sensing range and 4.0% response at 100 ppm. A similar system was investigated by Yin et al. (2018)[22] but using reduced graphene oxide (rGO) coated with polypyrrole nanofiber (PPy–rGO). After in-situ synthesis of CuBTC with PPy–rGO, the composite was prepared into the slurry in DMF and drop coated on Indium tin

[a] Univ. Grenoble Alpes, CNRS, Grenoble INP[e], LGP2, F-38000 Grenoble, France.
[b] Welsh Centre for Printing and Coating, College of Engineering, Swansea University, Swansea, SA1 8EN, UK.
[c] Centre for NanoHealth, College of Engineering, Swansea University, Swansea, SA2 8PP, UK.
[d] Nestle Research Center, 1000 Lausanne, Switzerland
[e] Institute of Engineering Univ. Grenoble Alpes
* Corresponding author, Dr. Zari Tehrani, Centre for NanoHealth, College of Engineering, Swansea University, Swansea, SA2 8PP, UK, z.tehrani@swansea.ac.uk
† Electronic Supplementary Information (ESI) available: Details of methods and characterization. See DOI: 10.1039/x0xx00000x

oxide (ITO) substrate. The sensors displayed selective (compared to hydrogen sulphide, ethanol, hydrogen, methane, and acetone) and reversible sensing range from 10 to 150 ppm at room temperature with 12.4% response for 50 ppm ammonia concentration. Bhardwaj et al. (2018) also took advantages of adding a conductive polymer into MOF/graphene derivative systems and prepared a three-component composite with rGO, silica coated CuBTC and polyaniline (PANI)[23]. CuBTC was prepared in situ with tetraethyl orthosilicate to form silica coated CuBTC particles to improve aqueous stability, mixed with rGO and aniline was finally polymerized in-situ with the rGO/silica coated CuBTC mixture. The sensors were prepared by drop-casting an ethanol suspension onto a 4-probe chromium electrode. The performances of the sensors at room temperature were found to be very interesting with a low detection limit (1 ppm) and a strong gas response (10% at 1 ppm), for a 1-100 ppm linear window. Finally, Ko et al. (2017) investigated sensors based on graphite and different hexahydroxytriphenylene (HHTP) derived MOFs, achieving response around 4% at 80 ppm with a 5-80 ppm linear range[24]. The innovation of their research was the sensor production process which was mechanical abrasion on a paper substrate.

The MOF/micro- and nano-carbon systems investigated in the literature requires in-situ and complex chemical synthesis[21–23], or use MOFs that are not commercially available[24]. A significant research challenge using these MOF/micro- and nano-carbon systems, is the development of facile and straightforward preparation of sensors, with strong sensing characteristic (sensitivity, selectivity, stability, fast response and recovery). In this work, a composite CuBTC/carbon-graphene ink was prepared by simple mixing of the commercially supplied components, and requires no small batches complex chemical synthesis. This straightforward preparation of the sensors, using active suspensions prepared by simple mixing from ready-to-use materials, has significant benefits in terms of industrialization up-scaling or commercialization. Moreover, it provided the opportunity to prepare the devices on a flexible polymer substrate, fit for smart packaging applications. Only a few recent examples (2019) in the literature has reported the use of flexible polymer substrates for electrical gas sensors based on MOF materials, and none for the detection of ammonia[14,17].

Inks with different ratios of CuBTC/carbon-graphene were formulated and drop-casted on screen-printed silver interdigitated electrodes. The surface properties of the sensors were investigated as well as their electrical gas sensing (sensitivity, stability, kinetics) capability using a custom-built gas rig capable of achieving controlled gas concentration down to ppm levels[25]. Finally, an investigation of the surface chemical properties of the devices was also performed before and after exposition to ammonia to provide insight into the sensing impact of the chemical stability of the devices.

2. Experimental

View Article Online
DOI: 10.1039/D0TC04553E

2.1. Materials and reagents

For a substrate, 175 µm Melinex 339 polyester film was purchased from DuPont Teijin Films (USA), the AST 6025 silver ink and the C2171023D1 carbon-graphene ink from Sun Chemicals (USA), the copper benzene-1,3,5-tricarboxylate (CuBTC) Metal Organic Framework (MOF) from MOF Technologies (UK) having a BET surface area of 1781 $m^2.g^{-1}$ and mean pore diameter of 1.5069 nm as supplied by the manufacturer, and analytical reagent grade n-butyl acetate from Fisher Scientific (UK). The materials were used as received.

2.1. Gas sensor fabrication

2.1.1. Fabrication of electrodes by screen-printing.

An interdigitated electrode (IDE) design was used to optimize the total conductive sensing surface[26,27], and the design is shown in the **Fig. 1**. The IDEs were printed with silver paste using an R29 series screen printer from Reprint using the following parameters: 50 $mm.s^{-1}$ forward speed, 10 $mm.s^{-1}$ reverse speed, 5.0 kg front squeegee pressure and 2.0 mm print gap. The printed IDEs were oven-dried for 30 min at 100°C. Polyester

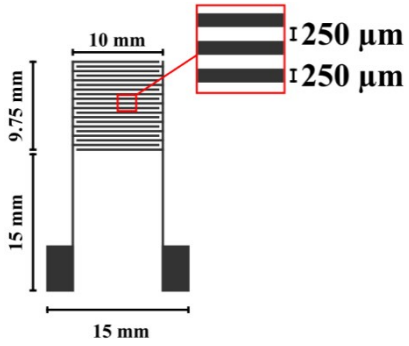

Fig. 1 Schematic representation of the interdigitated design and associated metrics.

screen with a 120-34 mesh was used and based on its specification (**ESI†**, **Table SI 1**), the expected target wet thickness was 15 µm. The screen printing process was chosen because of the high reproducibility and manufacturing scale-up potential for printed electronics applications[28,29].

2.1.2. Ink Formulation.

Inks (or can also be called slurries) suitable for drop casting were prepared by weighing the desired mass of the two components and mixing them in butyl acetate solvent to reach the final desired concentration. A vortex mixing technique at room temperature was used three times for 30 s because it was found to visually disperse the materials properly to make the inks for deposition. All of the inks were based on a 200 $mg.mL^{-1}$ concentration of MOF with the corresponding dry carbon-graphene (35% mass content commercial ink) mass added to reach inks with different ratios. The first control inks (MOF only) was prepared by dispersing 200 $mg.mL^{-1}$ of MOF dry powder in butyl acetate with the same mixing procedure and the second control ink (carbon-graphene only) was prepared by dispersing 54 $mg.mL^{-1}$ dry of the commercial ink in butyl acetate. Within this work, the sensors produced are referred to as PGrCuBTC X with X as the mass percentage of graphene in the ink, for

View Article Online
DOI: 10.1039/D0TC04557B

instance: PGrCuBTC 21.25 is the ink with 21.25%wt carbon-graphene/78.75%wt MOF. The composition of each ink is detailed in the **ESI†** (**Table SI 2**).

2.1.3. Deposition of active material on the electrode

The 8 µL of ink formulated was drop-casted on the printed IDE with a micropipette, aiming to cover the electrodes completely, followed by oven-drying at 100°C for 30 min. At least four devices using the same ink formulation were prepared and the deposited mass was measured (average is presented with standard deviation) (**Table 1**).

Table 1 Mass (mg) of CuBTC/carbon graphene ink deposited on screen printed IDE for each formulation.

Formulation name (PGrCuBTC) %	Mass of ink drop-casted (mg)
0 (control): CuBTC	1.70 ± 0.53
20	1.65 ± 0.21
21.25	2.37 ± 0.42
22.5	1.77 ± 0.32
25	1.85 ± 0.50
30	1.30 ± 0.34
50	1.90 ± 0.90
100 (control): carbon-graphene	N.A.

The quantity of ink deposited on the electrodes is relatively similar for each formulation and with expected standard deviation considering the small amount deposited and the manual drop-casting deposition technique.

2.2. Characterization Techniques

The pristine IDE was characterized using a White light Interferometer Veeco Wyco NT9300 at ×5 magnification and 736 × 480 pixels resolution with a 1.2 mm x 0.93 mm measured area. The thickness was measured by the difference between the substrate while excluding the print edges. At least 20 different samples were tested with four measurements on each, and the average results along with standard deviation are summarized in **Table 2**. The obtained thickness is close to the target (15 µm), and the lines show very good consistency: the deviation from the target geometry is a well-known characteristic of the process that may be compensated for if necessary[30].

Table 2 Summary of the pristine IDE morphology parameters measured by White Light Interferometry.

Digit thickness (µm)	Digit widths (µm)	Interspacing (µm)
14.7 ± 1.1	275.6 ± 19.0	227.0 ± 19.3

The same measurement parameters were used to investigated the drop-casted layers and the thicknesses were measured by the difference between substrate and deposited layer measured between the silver lines. The average surface roughness (Sa) of the samples was also measured at three different locations on the drop cast surface and four different sensors were tested. The average is presented along with the standard deviation in **Table 4** and discussed in the Results and Discussion section.

X-ray diffraction spectra were obtained on a Bruker D8 Discover apparatus equipped with Cu source (α=1.5406 Å). A Kratos Axis Supra XPS equipped with an Al Kα X-Ray monochromatic source was used to conduct the X-ray photoelectron spectroscopy (XPS) experiments at 15 mA emission current, with a pass energy of 20 eV.

Scanning electron microscopy (SEM) pictures were recorded on a Hitachi S4800 with 2.5 kV acceleration voltage, 20 µA emission current and a working distance of 11.9 mm. The atomic force microscopy (AFM) experiments were performed on a JPK NanoWizards II equipment (Dimension-3100 Multimode) from Bruker. A non-contact AFM tip (radius 8 nm) was used at 320 Hz using a spring constant of 40 N/m on AC mode. The SEM equipment was used coupled with an Energy Dispersive X-Ray analyzer (EDX) X-MAX 50mm² from Oxford Instrument to measure the atomic weight distribution (%) for each element and the measurements were performed on images taken at the same parameters settings as the SEM imaging above with 120 s collection.

Fourier-transform infrared (FTIR) measurements were conducted at room temperature on Bruker Alpha P equipment using Universal ATR detector from 400 to 4000 cm^{-1} at a 2 cm^{-1} resolution and a total of 16 accumulated scans. The Raman experiments were performed on a Renishaw apparatus coupled with a 532 nm wavelength excitation laser at 0.03 mW power and acquisition time of 20s for PGrCuBTC 0 and PGrCuBTC 21.25 at 0.15 mW power and acquisition time of 10s for PGrCuBTC 100. For both FTIR and Raman experiments, no baseline correction and no normalization were conducted, but the different spectra were shifted along the Y-axis to facilitate the reading and interpretation.

Current-voltage (I/V) curves were recorded using a two-probe SemiProbe I/V (SemiProbe MA-8005 manipulator) connected to a 2612B Keithley Source Meter: a sweeping mode from -1.0 to 1.0 volts with 100 measurements point was used and the source limit and source range was adjusted between 10 µA and 1 A depending on the devices. The resistance was calculated by measuring the corresponding I/V curve slope. The same I/V measurements were also performed on two PGrCuBTC 21.25 sensors after preparation (t=0) and after storage time (in sealed boxes, t=10 months) to investigate the time stability of the devices. The silver lines (connecting the digits to the pads) were covered with D2140114D5 dielectric paste from Gwent Chemicals to avoid extensive oxidation).

The gas sensing experiments were conducted at room temperature (ca. 20-22°C), and using pure Nitrogen 293679-L (>99.9995%) and pure Oxygen 284915-V (>99.999%) from BOC as carrier gas, mixed with a ratio 4:1 to model air composition independently of the total flow rate used. 298610-AK-B dry ammonia (H_20 < 200 ppm according to manufacturer) from BOC was used as the gas target, and a detailed description of the custom-built gas sensing equipment can be found in the **ESI†** (**Figure SI 1**). Only the response to dry ammonia concentration was investigated under dry atmosphere. Prior to sensing, the

View Article Online
DOI: 10.1039/D0TC04553E

Table 3 Summary of the experimental parameters used during the gas sensing tests.

	Concentration (ppm)	Increment (ppm)	Steps time in/out (min)	Total flow (sccm)	Stabilization step time/flow (min/sccm)
High range	50-500	50	60/60	200	120/1000
Low range	20-100	20	30/30	1000	60/1000

sensors were wired and connected from the inside of the gas chamber to a Keithley 6487 meter to follow their resistance against ammonia input (**ESI†**, **Figure SI 2**). Gas sensing tests were carried out with two different sets of parameters (high and low range) to fit the linear range of the sensors. For both sets of parameters, acquisition time was set at 1 s. The sensors were first flashed in a stabilization step to stabilize their resistance under dry airflow and then successively exposed to dry ammonia and dry air with an increasing ammonia concentration. The different parameters used are summarized in **Table 3**.

The sensors response (%) was calculated for each step of the experiment using equation **(1)**:

$$Response\ (\%) = 100 \times \frac{R_p - R_0}{R_0} \quad \textbf{(1)}$$

Where R_0 (Ω) is the resistance of the device at the beginning of ammonia input for the desired step and R_p (Ω) is the resistance of the device on the plateau (averaged for 600 s for the High range and 300 s for the Low range). For each step, the response time (s) was calculated as the time during the NH_3 input to reach 90% of the plateau resistance and the recovery time (s) as the time during the NH_3 output necessary to recover 90% of the baseline resistance value. Finally, the sensitivity of the sensor was defined by the slope of the response (%)/concentration (ppm) calculated by the linear fitting. At least two sensors from each formulation were tested and the average along with standard deviation is presented. An additional test under humidity was also performed by fitting a bubbler on one of the gas lines and estimating the approximate relative humidity using the flow ratio between "wet" and "dry" lines.

3. Results and discussion

3.1. Characterization of carbon-graphene electrode with CuBTC (PGrCuBTC)

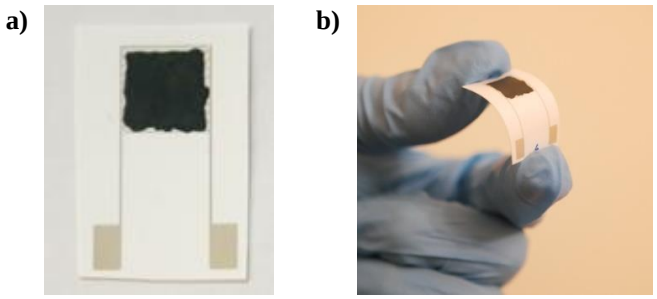

Fig. 2 Representation of the prepared devices with **a)** picture of one PGrCuBTC sensor prepared by drop-casting CuBTC/carbon-graphene ink on silver interdigitated electrode **b)** evidence of device flexibility.

3.1.1. Surface topography and electrical properties.

Different ink formulations were prepared and drop-casted on the screen-printed silver interdigitated electrodes. Within this work, the ratio between CuBTC and carbon-graphene component was varied and the sensors produced are referred as PGrCuBTC X with X the mass percentage of graphene in the ink, for instance: PGrCuBTC 21.25 is the ink with 21.25%wt carbon-graphene/78.75%wt MOF. The drop-casting process is straightforward and was used because of the small volume necessary for the formulation and thus the economy of materials. A typical example of the prepared devices can be seen in **Fig. 2a** along with a display of the flexibility of the sensor (**Fig. 2b**).

The thickness and the surface roughness of the sensors was then measured (**Table 4**).

Table 4 Summary of the thickness (µm) and surface roughness (Sa, µm) measured by White Light Interferometry, for the different sensors prepared.

Formulation name (PGrCuBTC) %	Electrode thickness (µm)	Electrode roughness (Sa, µm)
0 (control): CuBTC	45.79 ± 2.56	15.68 ± 3.16
20	32.62 ± 0.90	10.47 ± 2.26
21.25	31.95 ± 3.04	9.25 ± 1.95
22.5	36.19 ± 5.64	12.58 ± 3.48
25	27.15 ± 6.99	6.01 ± 2.16
30	34.94 ± 5.91	7.09 ± 3.55
50	24.82 ± 10.18	8.27 ± 4.62
100 (control): carbon/graphene	3.05 ± 0.28	4.62 ± 0.46

PGrCuBTC 0 (only CuBTC) displays the largest thickness and roughness and an increasing quantity of carbon-graphene in the ink formulation reduces the thickness and also the roughness. The mechanisms that influence this are not clear, but it could be suggested based on previous work that adding carbon-graphene into the formulation reduces the CuBTC aggregation because of enhanced dispersive forces[31] and so leading to a reduced thickness and roughness. However as shown in **Fig. 4c**, PGrCuBTC 21.25 retains some elements of surface roughness when compared with PGrCuBTC 100 and this is important in sensing application as it effectively increases the surface area available for sensing.

The carbon-graphene added into the formulation is necessary to confer conductivity to the deposited layer, because of the insulating nature of the CuBTC. The ratio of the raw materials in the ink was then modified to optimize the electric properties of the sensors as a compromise between the absorption capability of the MOF and layer conductivity to

View Article Online
DOI: 10.1039/D0TC04557E

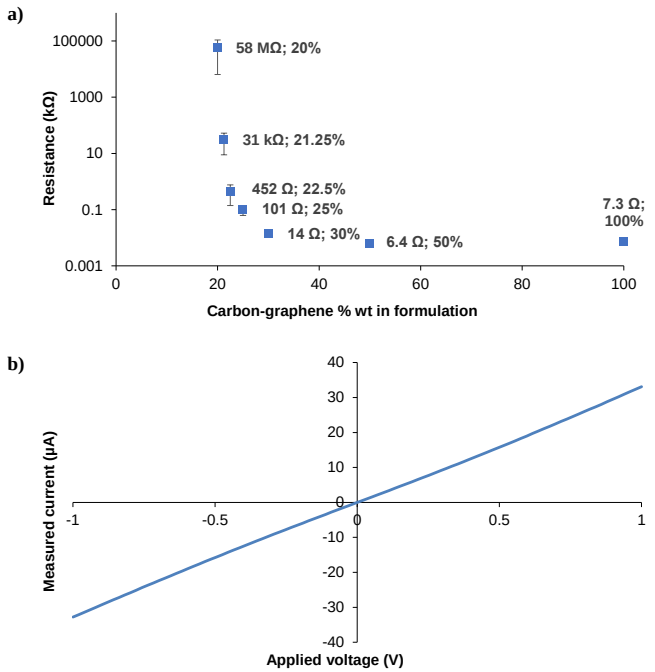

Fig. 5 Electrical properties of the sensors with **a)** resistance (Ω) of the sensors compared to the mass percentage of carbon-graphene in the ink formulation and **b)** Current/Voltage curve of PGrCuBTC 21.25.

detect the change in electrical signal of the CuBTC layer when exposed to the gas target. The resistance of the sensors was measured and found to be strongly formulation dependent (**Fig. 3a**). Beyond 50% wt of carbon-graphene in the formulation, the resistance of the devices is around 6-7Ω and does not vary with the concentration attributed to saturation of the percolating network formed by the carbon-graphene content. Also, the sensors are not conductive below 20% wt of carbon-graphene (>50MΩ) which may be explained because the concentration is now below the percolation threshold. Surprisingly the evolution of resistance is not linear and the resistance change is significant at the carbon-graphene concentration in the 21.25-25% wt range. Indeed, the resistance of PGrCuBTC 21.25 is 68 times higher than PGrCuBTC 22.5. Also, the lower the concentration of carbon-graphene inside the ink, the more difficult it is to prepare sensors in a reproducible manner due to high sensitivity of resistance to carbon-graphene content. PGrCuBTC 21.25 was then chosen to be most appropriate because of the lower content of carbon-graphene within the ink while retaining a measurable conductivity i.e the carbon-graphene does not mask the MOF detection capability. The current/voltage curve of PGrCuBTC 21.25 shows its ideal resistor behaviour makes it fit for reliable sensing independently of the voltage applied (**Fig. 3b**).

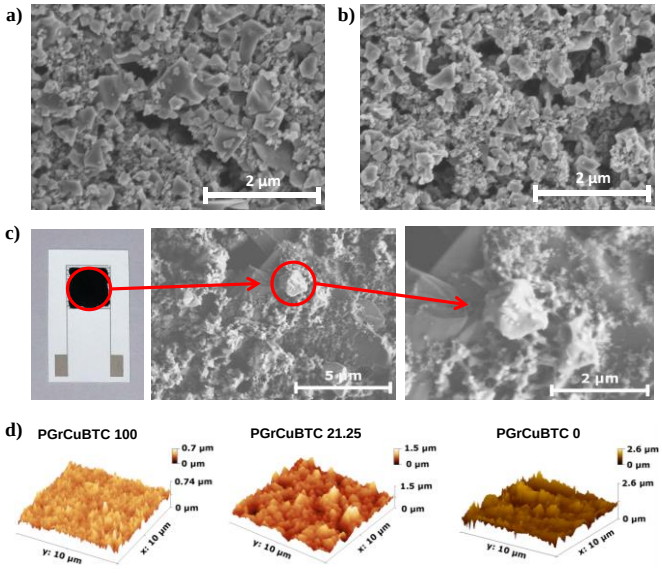

Fig. 3 Surface topography of the prepared sensors with **a) and b)** 2 SEM pictures of the surface of PGrCuBTC 21.25, **c)** SEM picture of the surface of PGrCuBTC 21.25 with zoom on one CuBTC crystallite and **d)** AFM images of the surface of PGrCuBTC 0, PGrCuBTC 21.25 and PGrCuBTC 100.

3.1.2. Microscale topography

On the Scanning Electron Microscope (SEM) images of the surface of PGrCuBTC 21.25 (**Fig. 4a and b**), it is possible to distinguish the population of CuBTC crystals due to their distinctive shape. The **Fig. 4c** shows a zoom on one specific crystal sitting on the graphitic platelet, confirming the spatial interaction between the two materials. Images of the control PGrCuBTC 0 and 100 are available in the **ESI†** (**Figure SI 3**). SEM coupled with Energy Dispersive X-Ray analyser (SEM-EDX) mapping (**ESI†**, **Figure SI 4**) also shows the proper dispersion at the microscale of the copper element, proving the proper dispersion of the CuBTC. SEM-EDX mapping was also performed for the sensors prepared with the different formulations (**ESI†**, **Figure SI 5**). The surface atomic weight (%) measured by SEM-EDX for carbon, oxygen and copper elements was found to be linearly correlated with the content of carbon-graphene in the ink, again confirming the good dispersion of the ink components during the formulation and deposition on the electrodes. The surface of the controls and PGrCuBTC 21.25 were also imaged by Atomic Force Microscopy (AFM) and for PGrCuBTC 0 (MOF only), it appears random and heterogeneous (**Fig. 4d**). This might be due to some CuBTC aggregation that leads to a more heterogeneous surface. The surface of PGrCuBTC 100 also appears rough but with a small maximum height due to the small size of the carbon particles. On the other hand, the surface of PGrCuBTC 21.25 is smoother with a higher maximum height

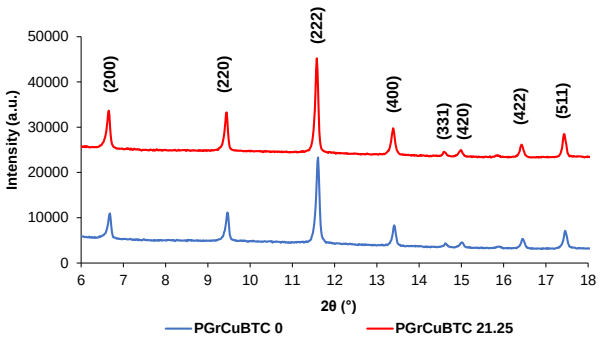

Fig. 4 X-ray Diffraction of the surface of PGrCuBTC 0 and 21.25.

compared to PGrCuBTC 100. This is consistent with the addition of micro-particles such as MOF crystallites.

3.1.3. Surface chemistry

X-ray Diffraction (XRD) was performed on the surface of the PGrCuBTC 0 and PGrCuBTC 21.25 (**Fig. 5**). The characteristic peaks of CuBTC at small angles can be seen on PGrCuBTC 100 in the 6-18° region as described in the literature[32–34] which indicates that dispersing CuBTC into butyl acetate and drop-casting on the screen-printed silver IDE does not impact its crystallinity. Moreover, the XRD pattern of PGrCuBTC 21.25 is similar to PGrCuBTC 100 which also indicates that mixing with the carbon-graphene component does not alter the crystallinity of the MOF. This proves that the crystalline structure of the CuBTC, which is a key factor for its gas sensing properties, is not affected by the sensor preparation.

The surface chemistry of the devices was then investigated using Fourier-transform infrared (FTIR) and Raman spectroscopy (**Fig. 6**). Concerning FTIR results (**Fig. 6a**), the PGrCuBTC 0 display the classic peaks of CuBTC[35–37]: the Cu-O stretching band at 490 cm^{-1}, the aromatic C-H (out of plane) deformation bands at 730 cm^{-1} and 761 cm^{-1}, the C-H aromatic stretching band at 1112 cm^{-1}, the COO symmetric stretching band at 1372 cm^{-1}, and the corresponding asymmetric bands at 1448 cm^{-1} and 1648 cm^{-1}. The peaks at 1709 cm^{-1}, 1280 cm^{-1} and the slight shoulder at 1618 cm^{-1} and 1254 cm^{-1} seem to indicate the presence of a small quantity of a free benzene-1,3,5-tricarboxylic acid ligand[38,39]. As expected only small and not well-defined signals can be seen on the PGrCuBTC 100 spectrum as carbon and graphene materials have high refractive index which is relatively close to the diamond value thus making ATR FTIR difficult[40]. The PGrCuBTC 21.25 spectrum is the superposition of the PGrCuBTC 0 and PGrCuBTC 100 spectra in proportions confirming the proper mixing and dispersion of the materials at the surface of the devices. On the Raman spectra

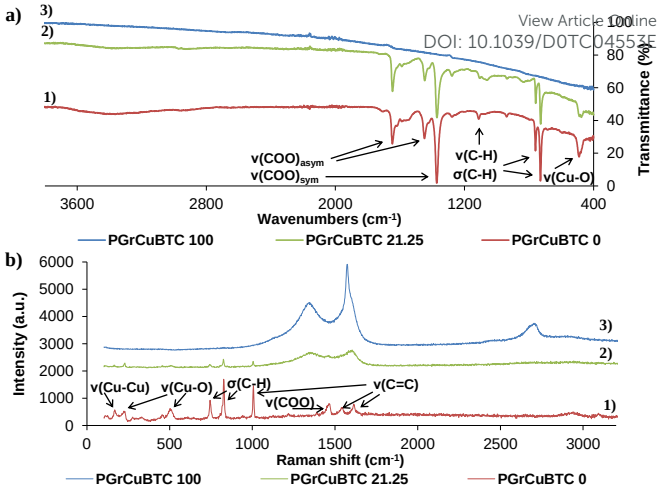

Fig. 6 Surface chemistry investigation of the produced sensors with **a)** FTIR spectra of the PGrCuBTC 0 **(1)**, 21.25 **(2)** and 100 **(3)** samples, and **b)** Raman spectra of the PGrCuBTC 0 **(1)**, 21.25 **(2)** and 100 **(3)** samples.

of PGrCuBTC 0, the following CuBTC characteristic peaks can be noted (**Fig. 6b**)[41,42]: the Cu-Cu dimer stretching band at 177 cm^{-1}, the Cu-O stretching bands at 283 cm^{-1}, 449 cm^{-1} and 507 cm^{-1}, the aromatic C-H out of place deformation bands at 746 cm^{-1} and 829 cm^{-1}, the C=C aromatic stretching bands at 1009 cm^{-1}, 1549 cm^{-1}, and 1618 cm^{-1}, the COO symmetric stretching at 1391 cm^{-1} and the corresponding asymmetric band at 1468 cm^{-1}. For the PGrCuBTC 100 sample, the 1360 cm^{-1} band can be attributed to the D band, the 1575 cm^{-1} to the G band and the slight shoulder on the latter to the D' band. Finally, a small 2D band can be found at 2710 cm^{-1}. The obtained spectrum is typical of a mixture of carbon and graphene materials[43,44]. As for the FTIR spectra, the PGrCuBTC 21.25 is the superposition of the PGrCuBTC 0 and 100; leading to the same conclusion.

To confirm this trend, X-ray photoelectron spectroscopy (XPS) experiments were also performed on PGrCuBTC 0, 21.25

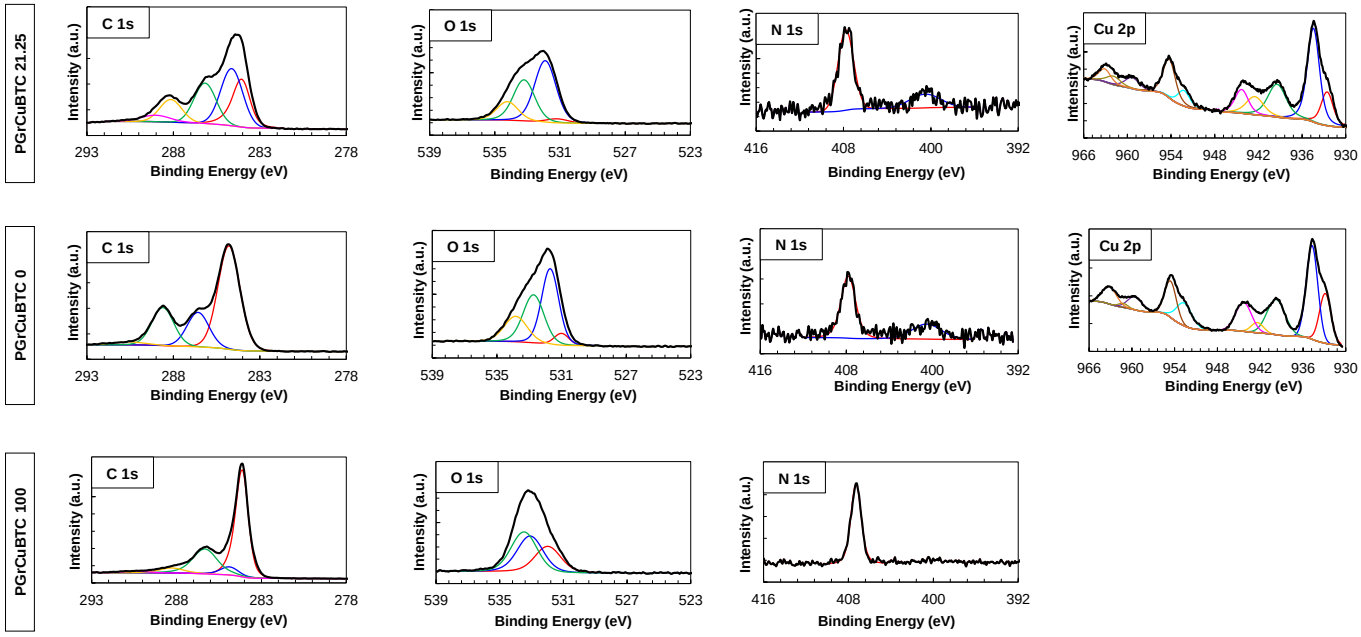

Fig. 7 X-ray photoelectron spectroscopy of PGrCuBTC 100, 0 and 21.25 with the detected atoms, the measured response and fitting of the attributed peaks.

View Article Online
DOI: 10.1039/D0TC04557F

and 100 (**Fig. 7**). The elemental concentration for each device matches the expected elements, meaning mainly carbon and oxygen for PGrCuBTC 100, and carbon, oxygen and copper for PGrCuBTC 0 and 21.25 (**ESI† – Table SI 3**). A relatively low amount of chlorine was found in all samples which was attributed to environment contamination whereas residual nitrogen was attributed to additives present in the carbon-graphene materials[45] and residual nitrate from CuBTC synthesis.

PGrCuBTC 100 spectra fit well with the corresponding literature and especially in the C1s spectra: C-C (59.58%), C=C (6.55%), C=O (26.85%), C-O (5.38%) and O-C=O (1.64%) peaks respectively at 284.09, 284.89, 286.3, 288.28 and 290.4 eV are common attribution for graphene and carbon materials[45–48]. These are reflected in the O1s spectra as C=O (25.76%) and C-O (35.35) peaks respectively present at 531.98 and 533.08 eV and a peak at 533.47 eV was attributed to the NO_3 (38.88%) bond relative to the nitrocellulose additive in the commercial ink[49]. In the C1s region of the PGrCuBTC 0, C-C (57.32%), C-O (19.12%) and C=O (21.09%) peaks respectively at 284.79, 286.57 and 288.61 eV are the main attribution for CuBTC materials as described previously[50,51]. A smaller peak relative to O-C=O (2.47%) bond can be found at 290.59 eV which was attributed to a low amount of free BTC ligand[52]. In the O1s spectra, the C-O (32.80%) and C=O (42.41%) peaks (respectively 532.73 and 531.70 eV) match the C1s spectra whereas a NO_3 (19.02%) was found at 533.83 eV, associated with nitrate-based impurities.

Finally, a small peak at 531.00 eV attributed to the CuO (5.77%) bond showed that the CuBTC presents impurities linked to its synthesis which is further confirmed by the presence of nitrate peak (68.24%) in the N1s spectra at 407.81 eV[53]. The Cu 2p region is also in accordance with literature, showing mainly Cu(II) peaks at 934.73 and 954.57 eV (respectively 26.35% and 10.08%) and minor presence of Cu(0) and Cu(I) at 932.88 and 952.67 eV (respectively 14.01 and 8.63%)[54,55]. The detailed peaks attribution, binding energy and atomic concentration can be found in the **ESI†** (**Table SI 4**, **Table SI 5**, **Table SI 6**). Finally, the PGrCuBTC 21.25 spectra for all detected elements are in accordance with the mixing of both CuBTC 0 and 100 with the applied ratio. The XPS experiments proved the presence and chemical structure of the expected carbon-graphene and CuBTC materials corresponding to relevant literature.

To summarize this section, it was first found that adding more carbon-graphene materials to the CuBTC materials reduces the thickness and roughness of the produced sensors, probably because it improves the dispersion of CuBTC and thus reducing aggregation of crystals. The electrical properties of the devices were then found to be highly formulation-dependent and PGrCuBTC 21.25 was chosen as the optimized formulation because of the lowest carbon-graphene content while being still conductive enough for reliable measurements. For this formulation, SEM imaging showed the interaction of CuBTC crystal with carbon-graphene materials and AFM measurements confirmed the macro-scale morphological investigation. XRD experiments also showed that the crystalline structure of CuBTC was retained through the formulation and deposition on the substrate. The surface chemistry of the sensors was investigated and using SEM-EDX mapping, the atomic weight (%) of carbon, oxygen and copper was found to be linearly correlated with the composition of the formulation which means that the dispersion of the materials is good. FTIR and Raman spectroscopy showed that PGrCuBTC 21.25 spectra are the superposition of PGrCuBTC 0 and 100 spectra adding further confirmation that there is proper dispersion and good mixing between the two components. Finally, XPS experiments also proved that the chemical structure of the sensors is correlated with the materials used in accordance with appropriate literature.

3.2. Gas sensing

The different sensors produced were tested against ammonia sensing in dry conditions, initially from 50 to 500 ppm (high range, see *Experimental* section). The complete evolution of the sensor's behaviour can be found in the **ESI†** (**Figure SI 6 a-d)** while the **Fig. 8a** shows the comparative response of the sensors at 500 ppm (using the normalized resistance). **Fig. 8b** also shows that the response for each step is nonlinear with the ammonia concentration throughout this range. This graph can be differentiated into two sections having a breakpoint at 150 ppm, which suggest saturation of the sensors. That is why the responses of the sensors were investigated in more details over the range 20-100 ppm (low range, see *Experimental* section) and the complete evolution of the sensor's behaviour over this range can be found in the **ESI†** (**Figure SI 6 e-h)** while the **Fig. 8c** shows the comparative response of the sensors at 100 ppm (using the normalized resistance). The slight difference in response at 100 ppm for the two ranges could be explained by the significant change in the flow rate used. The PGrCuBTC 25, 22.5 and 21.25 all displayed good linear fitting in the 40-100 ppm range (**Fig. 8d**). Surprisingly PGrCuBTC 21.25 is the only sensor to achieve good sensing at 20 ppm. PGrCuBTC 50

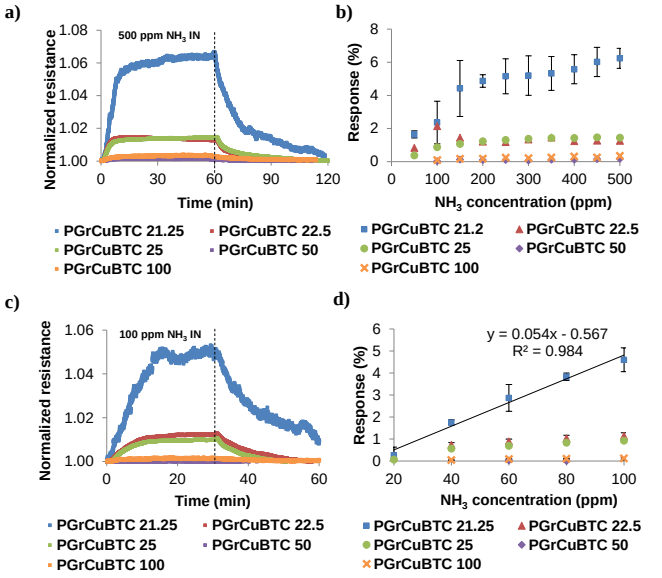

Fig. 8 Gas sensing experiments with **a)** normalized resistance evolution for the different sensors when exposed to 500 ppm of NH_3, **b)** summary of the response (%) for the different sensors for the high range (50-500 ppm NH_3), **c)** normalized resistance evolution for the different sensors when exposed to 100 ppm of NH_3 and **d)** summary of the response (%) for the different sensors for the low range (20-100 ppm NH_3).

displayed no proper response because of the resistance stabilization due to carbon content being more dominant than the sensing response attributable to the MOF. For clarity purposes, only the trend line of PGrCuBTC 21.25 is displayed in **Fig. 8d** with the other device results presented in the **ESI†** (**Figure SI 7**) along with their linear trend lines. The sensing results for each sensor are summarized in **Table 5**, for parameters including sensitivity (%.ppm^{-1}), and response (%) at 100 ppm and the coefficient of determination for linear fit from either 20 to 100 ppm for PGrCuBC 21.25 and 40 to 100 ppm for all other sensors.

Table 5 Summary of the sensing parameters for all PGrCuBTC sensors for the 20-100 ppm range.

Formulation name PGrCuBTC	**21.25**	22.5	25	50	100 control
Sensitivity (%.ppm^{-1})	**0.0538**	0.0068	0.0060	-	0.0012
Coefficient of determination R²	**0.984**	0.993	0.993	-	0.912
Response at 100 ppm (%)	**4.60 ± 0.54**	1.14 ± 0.14	0.92 ± 0.1	-	0.12 ± 0.03

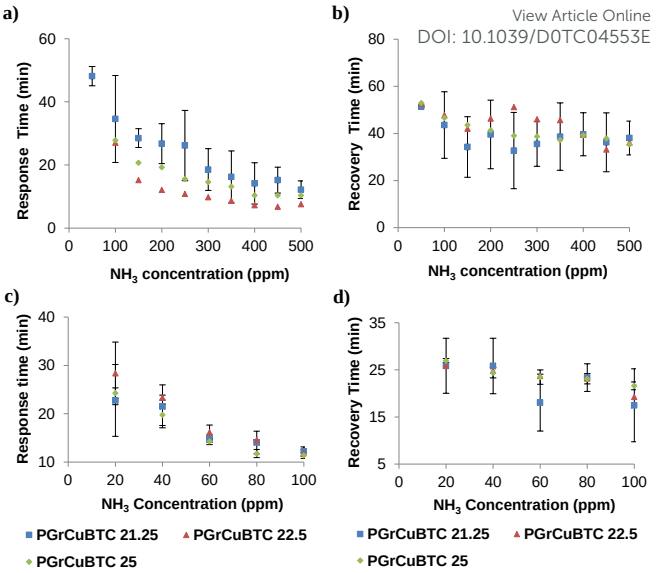

Fig. 9 Sensing kinetics of the PGrCuBTC 21.25, 22.5 and 25 sensors with **a)** response time (min) for the high range (50-500 ppm NH_3), **b)** recovery time (min) for the high range (50-500 ppm NH_3), **c)** response time (min) for the low range (20-100 ppm NH_3) and **d)** recovery time (min) for the low range (20-100 ppm NH_3).

PGrCuBTC 21.25 displayed the highest response (4.6%) and compared with PGrCuBTC 100 (only carbon-graphene), this is 36 times higher at 100 ppm, proving that the CuBTC is responsible for the gas sensing properties. Moreover PGrCUBTC 21.25 shows a sensitivity of 0.054 %.ppm^{-1}, which is 45 times more than for PGrCuBTC 100. It is however important to note that due to the drop-casting deposition process, a slightly higher mass was deposited on the electrodes for the PGrCuBTC 21.25 formulation (**Table 1**) and that this might have a small positive influence on the sensor's performance. Only a small change can be seen between the performances of PGrCUBTC 22.5 and PGrCUBTC 25.

The sensors characteristic times (response and recovery) were also extracted from the gas sensing results and are summarized in **Fig. 9**, but the graphs only show PGrCuBTC 21.25, PGrCuBTC 22.5 and PGrCuBTC 25 because PGrCuBTC 50 and 100 results were found to be erratic. For all sensors, recovery and response times are lower for the low range because of the increased flow rate during the experiments. The recovery time is nearly independent of the concentration of gas and is relatively similar for each sensor for either the low or high range. The response time, however, is concentration dependent: the higher the concentration, the lower the response time, and this is true for all PGrCuBTC 21.25, 22.5 and 25 sensors. Similar results have been reported and attributed to enhanced diffusion and reaction rate at higher gas concentration[56–58].

In summary, as expected from the electrical properties of the different sensors produced, the PGrCuBTC 21.25 showed the best gas sensing performances. For the first 50-500 ppm range, this sensor showed a response as high as 6.24% for 500 ppm. However, the behaviour of the sensor over this range was not linear, and a smaller 20 to 100 ppm range was tested. In this range, the sensors displayed a linear behaviour and with a response of 4.6% for 100 ppm for PGrCuBTC 21.25. The kinetics of the sensing was also investigated, and response time was found to be concentration-dependent, whereas recovery time was not. The **Table 6** summarizes the literature review discussed in the introduction and is focused only on MOF/micro- and nano-carbon systems whereas an extended version based on MOF materials for ammonia sensing can be found in the **ESI†** (**Table SI 7**).

Table 6 Literature review of ammonia sensors based on MOF/micro- and nano-carbon systems. (App.=approximate)

Sensor material	Material preparation	Device preparation (substrate)	Response (%, ppm)	Sensitivity (%.ppm^{-1})	Concentration range (ppm)	Ref.
Cu-BTC/graphite oxide	In-situ MOF synthesis	Coating suspension on Au IDE (ceramic)	4/100	App. 0.008	100-500	21
SiO_2 coated Cu-BTC/rGO/PANI	Synthesis of silica-coated CuBTC and in-situ aniline polymerization with graphene	Drop-casting suspension on 4 probe Cr electrode (N.A.)	144/100	1.39	1-100	23
Cu–BTC/PPy–rGO	In-situ MOF synthesis	Drop-casting suspension between copper foil strips (ITO)	20.3/100	App. 0.15	10-150	22
Graphite/$Cu_3(HHTP)_2$ Graphite/$Co_3(HHTP)_2$ Graphite/$Fe_3(HHTP)_2$ Graphite/$Ni_3(HHTP)_2$	MOF synthesis and ball-milling with graphite powder	Abrasion on Au IDE (paper)	4.6/80 4.2/80 4.0/80 2.9/80	App. 0.07 App. 0.07 App. 0.08 App. 0.06	5-80	24
Cu-BTC/carbon-graphene	**Simple mixing of commercial MOF and carbon-graphene**	**Drop-casting suspension on screen printed Ag IDE (PET)**	**4.6/100**	**0.054**	**20-100**	**This work**

View Article Online
DOI: 10.1039/D0TC04553E

The performances of the system developed in this work is in accordance with the literature yet on the low side of the range. However, compared to the literature, the straightforward formulation of active inks by simple mixing of commercially supplied components and its deposition onto a flexible polymeric substrate for the development of sensitive sensors is the key challenge addressed in this work. The results obtained in the work then show the strong potential of the developed solution to be industrially up-scale.

3.3. Stability

The stability of the sensor was first evaluated by investigating PGrCuBTC 21.25 response after five successive cycles at 500 ppm (**Fig. 10**). The tested sensor was stable over 5 cycles with only a 7% response loss.

To investigate the sensors' chemical stability after exposure to ammonia, FTIR and Raman spectroscopy were performed before and after exposition to 100 ppm of ammonia for 30 min for PGrCuBTC 0, 21.25 and 100. No changes could be seen on the Raman spectra and they are displayed in **Fig. 11**. However, some changes can be seen on FTIR spectra before and after sensing (**Fig. 12**) and especially for PGrCuBTC 0 (**Fig. 12c**). The main changes on the FTIR spectra of PGrCuBTC 0 before and after sensing are a significant increase in the intensity of already present peaks. Indeed, there is an increase of intensity for the characteristic peaks of the free benzene-1,3,5-tricarboxylate (BTC) at 1618 cm^{-1}, for the one at 1648 cm^{-1} and 1254 cm^{-1}. However, no increase in the free acidic peak at 1709 cm^{-1} can be seen. This could indicate that there is a change in the coordination of the BTC ligand but not corresponding to free BTC ligands. This tends to indicate a partial chemical reaction between ammonia and the BTC ligand, leading to $(NH_4)_3BTC$ and this is in agreement with previous literature on the subject, even if usually reported under humid conditions[59–61]. Even though the chemical nature of the sensors is not drastically modified after exposure to ammonia, the suggested reaction could have an impact on the long-time stability of the sensors and more work should be carried out to assess the lifetime of the developed sensors when used in some applications. However, for smart packaging applications, the sensors' stability is more linked to short term stability in application (preparation process, package incorporation, etc) rather than long-term cycling.

I/V measurement were also performed on two PGrCuBTC 21.25 sensors after storage time to investigate the time stability of the devices. After 10 months, only a small difference was noted in their resistance (respectively 20,097Ω and 32,287Ω at t=0 against 19,983Ω and 26,949Ω) and the shape of the I/V was also found to be unaltered by the storage (**ESI†, Figure SI 8**). It was then suggested than if the electrical properties of the sensors are unaffected by the storage, then the sensing performances should also not be affected. Although the influence of environmental humidity on the sensing performances was out of scope for this present study, a preliminary response-recovery test was performed using the

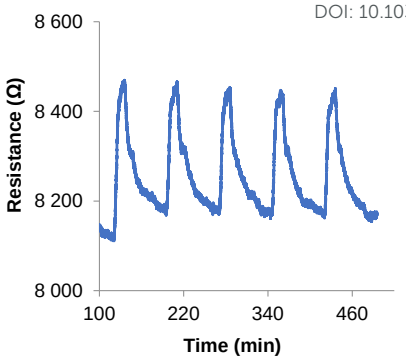

Fig. 10 Stability of the PGrCuBTC 21.25 sensor investigated by five successive cycles of 500 ppm NH_3 input and relaxation.

PGrCuBTC 21.25, at 100 ppm of ammonia under approximatively 90% of relative humidity. It proved that the sensor is indeed sensitive to humidity as the response drastically increased as shown in the **ESI† (Figure SI 9)**, yet more work is required to fully characterize the ammonia sensors under humid conditions. The CuBTC MOF is indeed known for presenting a low kinetic stability toward water than can prevent its use in environmental real-life conditions for sensing applications, however the timeframe of its stability under low humidity conditions (few weeks) could fit with the applications in smart packaging using an adequate calibration procedure [42,62,63]. Recent studies have also proposed techniques to impart hydrophobicity to CuBTC MOF and could be very interesting to achieve a water stable CuBTC for ammonia sensing under environmental conditions, such as active coatings, chemical

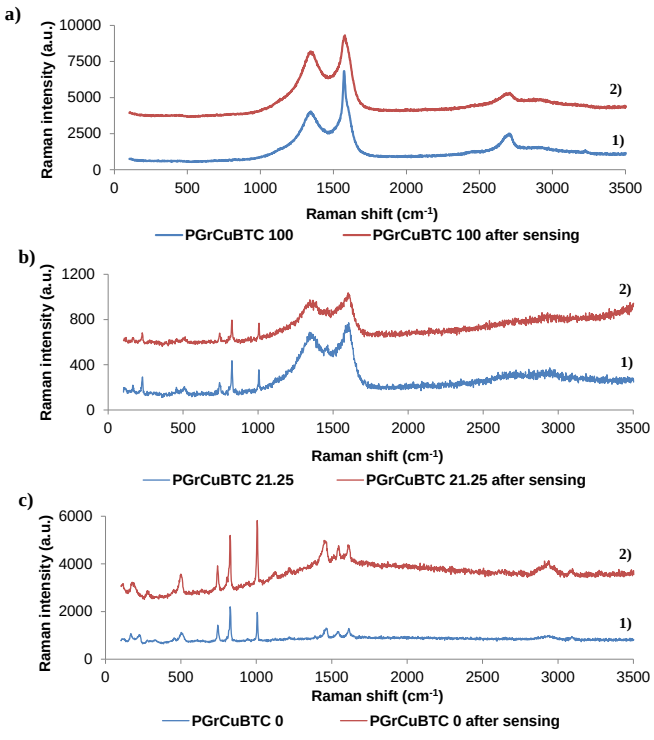

Fig. 11 Raman spectra before **(1)** and after **(2)** exposure to 100 ppm of NH_3 for 30 min for **a)** PGrCuBTC 100, **b)** PGrCuBTC 21.25 and **c)** PGrCuBTC 0.

View Article Online
DOI: 10.1039/D0TC04557F

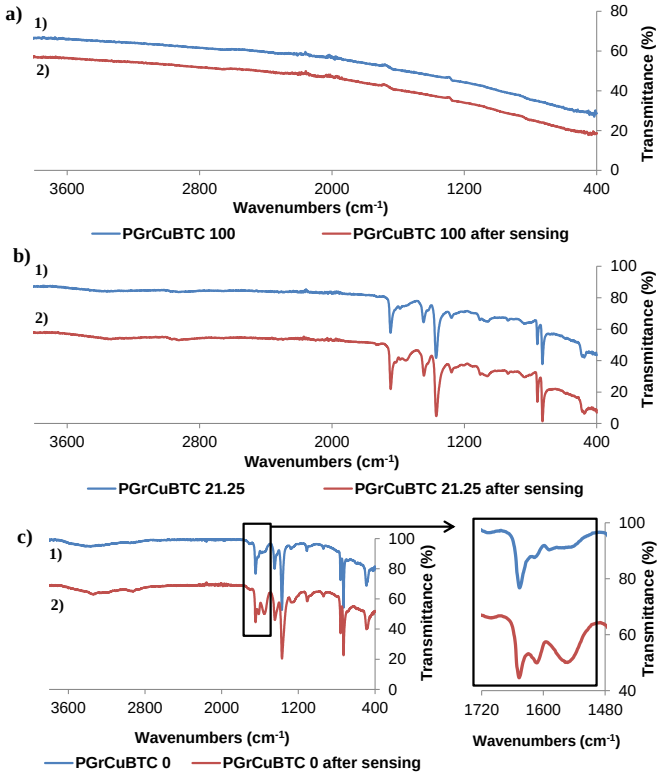

Fig. 12 FTIR spectra before **(1)** and after **(2)** exposure to 100 ppm of NH_3 for 30 min for **a)** PGrCuBTC 100, **b)** PGrCuBTC 21.25 and **c)** PGrCuBTC 0 with a zoom on the 1480-1720 cm^{-1} region.

functionalization or the use of additives to create composites (such as nanocarbons for instance)[64–67], offering promising solutions for the systems developed in this study to be used under less restrictive environmental conditions after a more in-depth characterization of their water-stability.

4. Conclusion

In this work, gas sensors were produced using metal organic framework and conductive carbon-graphene materials. Copper-based CuBTC metal organic framework and carbon-graphene conductive materials were formulated with different ratios and drop-casted on screen-printed silver interdigitated electrodes. Morphological analyses, microscale topography and surface chemistry investigation proved the consistency of the deposition process. The electrical properties of the sensors were highly formulation-dependent and the optimized devices were tested against ammonia gas sensing in dry conditions. The optimized devices displayed a low detection limit (20 ppm) and a linear range from 20 to 100 ppm. The sensor response was found to be as high as 4.6% with the optimized formulation which is 36 times higher than the only carbon-graphene blank sensor. The developed sensors also showed consistent results in short term stability tests. Compared to previous studies, this work proposes the development of sensitive ammonia sensors, based on the straightforward formulation of active inks by simple mixing of commercially available materials followed by their deposition on a flexible polymeric substrate. The simple preparation process and sensors' performance is a promising proof of concept for a potential industrial scale-up, which could be achieved by fully printing the entire sensors' architecture. Noting MOF response to water, the sensors could be used in smart packaging applications where humidity is controlled such as modified atmosphere packaging. Further investigations can be conducted to increase the sensitivity of the devices through investigation of other nanocarbon systems but also to assess the behaviour of the sensor in humid environmental conditions; stability and selectivity are key challenges that could be research using overprinting of suitable selective overlays, thus enlarging the potential scope of applications for the developed solution.

Conflicts of interest

There are no conflicts to declare.

Acknowledgements

This research was supported by LabEx Tec 21 (Grant agreement No. ANR-11-LABX-0030). and the joint-financial support from Welsh Government and European Commission under European Regional Development Funds (ERDF) through Sêr Cymru II Fellowships (Project Number: 80761-SU100).

Authors want to thank Thierry Maffeis for the gas sensing equipment and expertise, Brent de Boode for the help with the Raman spectroscopy and X-ray diffraction measurements.

References

1 O. M. Yaghi, G. Li and H. Li, *Nature*, 1995, **378**, 703.
2 K. K. Gangu, S. Maddila, S. B. Mukkamala and S. B. Jonnalagadda, *Inorganica Chimica Acta*, 2016, **446**, 61–74.
3 M. S. Hosseini, S. Zeinali and M. H. Sheikhi, *Sensors and Actuators B: Chemical*, 2016, **230**, 9–16.
4 X. Wu, S. Xiong, Z. Mao, S. Hu and X. Long, *Chemistry – A European Journal*, 2017, **23**, 7969–7975.
5 K. Sel, S. Demirci, O. F. Ozturk, N. Aktas and N. Sahiner, *Microelectronic Engineering*, 2015, **136**, 71–76.
6 M. L. Aubrey, M. T. Kapelewski, J. F. Melville, J. Oktawiec, D. Presti, L. Gagliardi and J. R. Long, *Journal of the American Chemical Society*, , DOI:10.1021/jacs.9b00654.
7 M. E. DMello, N. G. Sundaram, A. Singh, A. K. Singh and S. B. Kalidindi, *Chem. Commun.*, 2019, **55**, 349–352.
8 S. Achmann, G. Hagen, J. Kita, I. M. Malkowsky, C. Kiener and R. Moos, *Sensors*, 2009, **9**, 1574–1589.
9 M. G. Campbell, S. F. Liu, T. M. Swager and M. Dincă, *J. Am. Chem. Soc.*, 2015, **137**, 13780–13783.
10 M. R. Tchalala, Y. Belmabkhout, K. Adil, K. N. Chappanda, A. Cadiau, P. M. Bhatt, K. N. Salama and M. Eddaoudi, *ACS Appl. Mater. Interfaces*, 2019, **11**, 1706–1712.
11 L. Sun, M. G. Campbell and M. Dincă, *Angewandte Chemie International Edition*, 2016, **55**, 3566–3579.
12 L. Zhu, L. Meng, J. Shi, J. Li, X. Zhang and M. Feng, *Journal of Environmental Management*, 2019, **232**, 964–977.

13 S. Fardindoost, S. Hatamie, A. I. Zad and F. R. Astaraei, *Nanotechnology*, 2017, **29**, 015501.

14 N. Jafari, S. Zeinali and J. Shadmehr, *J Mater Sci: Mater Electron*, 2019, **30**, 12339–12350.

15 G. Lin, H. Wang, X. Lai, R. Yang, Y. Zou, J. Wan, D. Liu, H. Jiang and Y. Hu, *Sensors and Actuators B: Chemical*, 2020, **303**, 127219.

16 D. Ding, Q. Xue, W. Lu, Y. Xiong, J. Zhang, X. Pan and B. Tao, *Sensors and Actuators B: Chemical*, 2018, **259**, 289–298.

17 D. Zhang, Z. Wu and X. Zong, *Sensors and Actuators B: Chemical*, 2019, **288**, 232–242.

18 D. Zhang, D. Wu, X. Zong and Z. Yang, *J Mater Sci: Mater Electron*, 2019, **30**, 11070–11078.

19 R. J. LeBlanc and T. A. Gill, *Canadian Institute of Food Science and Technology Journal*, 1984, **17**, 195–201.

20 E. Monique, 2005, 22.

21 N. A. Travlou, K. Singh, E. Rodríguez-Castellón and T. J. Bandosz, *J. Mater. Chem. A*, 2015, **3**, 11417–11429.

22 Y. Yin, H. Zhang, P. Huang, C. Xiang, Y. Zou, F. Xu and L. Sun, *Materials Research Bulletin*, 2018, **99**, 152–160.

23 S. K. Bhardwaj, G. C. Mohanta, A. L. Sharma, K.-H. Kim and A. Deep, *Analytica Chimica Acta*, 2018, **1043**, 89–97.

24 M. Ko, A. Aykanat, M. K. Smith and K. A. Mirica, *Sensors*, 2017, **17**, 2192.

25 A. R. Lewis, J. Náhlík, D. R. Jones and T. G. G. Maffeis, *Procedia Engineering*, 2016, **168**, 321–324.

26 J. Zhang, L. Huang, Y. Lin, L. Chen, Z. Zeng, L. Shen, Q. Chen and W. Shi, *Appl. Phys. Lett.*, 2015, **106**, 143101.

27 A. I. Daud, K. A. A. Wahid and W. M. Khairul, *Organic Electronics*, 2019, **70**, 32–41.

28 S. Khan, L. Lorenzelli and R. S. Dahiya, *IEEE Sensors Journal*, 2015, **15**, 3164–3185.

29 J. Oliveira, V. Correia, H. Castro, P. Martins and S. Lanceros-Mendez, *Additive Manufacturing*, 2018, **21**, 269–283.

30 C. Timothy, *Coatings*, 2015, **5**, 172.

31 Y. Zheng, S. Zheng, H. Xue and H. Pang, *Advanced Functional Materials*, 2018, **28**, 1804950.

32 S. S.-Y. Chui, S. M.-F. Lo, J. P. H. Charmant, A. G. Orpen and I. D. Williams, *Science*, 1999, **283**, 1148–1150.

33 Y. Chen, X. Mu, E. Lester and T. Wu, *Progress in Natural Science: Materials International*, 2018, **28**, 584–589.

34 N. Al-Janabi, P. Hill, L. Torrente-Murciano, A. Garforth, P. Gorgojo, F. Siperstein and X. Fan, *Chemical Engineering Journal*, 2015, **281**, 669–677.

35 X. Li, C. Li, C. Wu and K. Wu, *Analytical Chemistry*, , DOI:10.1021/acs.analchem.9b00556.

36 R. Rani, A. Deep, B. Mizaikoff and S. Singh, *Vacuum*, 2019, **164**, 449–457.

37 S. Lin, Z. Song, G. Che, A. Ren, P. Li, C. Liu and J. Zhang, *Microporous and Mesoporous Materials*, 2014, **193**, 27–34.

38 R. R. F. Fonseca, R. D. L. Gaspar, I. M. Raimundo and P. P. Luz, *Journal of Rare Earths*, 2019, **37**, 225–231.

39 N. Shi, G. Yin, M. Han, L. Jiang and Z. Xu, *Chemistry – A European Journal*, 2008, **14**, 6255–6259.

40 C. Bartlam, S. Morsch, K. W. J. Heard, P. Quayle, S. G. Yeates and A. Vijayaraghavan, *Carbon*, 2018, **139**, 317–324.

41 N. R. Dhumal, M. P. Singh, J. A. Anderson, J. Kiefer and H. J. Kim, *J. Phys. Chem. C*, 2016, **120**, 3295–3304.

42 N. Al-Janabi, H. Deng, J. Borges, X. Liu, A. Garforth, F. R. Siperstein and X. Fan, *Ind. Eng. Chem. Res.*, 2016, **55**, 7941–7949.

43 M. Pawlyta, J.-N. Rouzaud and S. Duber, *Carbon*, 2015, **84**, 479–490.

44 L. M. Malard, M. A. Pimenta, G. Dresselhaus and M. S. Dresselhaus, *Physics Reports*, 2009, **473**, 51–87.

45 A. Devadoss, R. Forsyth, R. Bigham, H. Abbasi, M. Ali, Z. Tehrani, Y. Liu and O. J. Guy, *Biosensors*, 2019, **9**, 16.

46 Y. Shao, G. Yin, J. Zhang and Y. Gao, *Electrochimica Acta*, 2006, **51**, 5853–5857.

47 S. Stankovich, D. A. Dikin, R. D. Piner, K. A. Kohlhaas, A. Kleinhammes, Y. Jia, Y. Wu, S. T. Nguyen and R. S. Ruoff, *Carbon*, 2007, **45**, 1558–1565.

48 S.-J. Choi, S.-J. Kim and I.-D. Kim, *NPG Asia Materials*, 2016, **8**, e315.

49 B. C. Beard, *Applied Surface Science*, 1990, **45**, 221–227.

50 S.-Y. Kim, A.-R. Kim, J. W. Yoon, H.-J. Kim and Y.-S. Bae, *Chemical Engineering Journal*, 2018, **335**, 94–100.

51 S. Han, R. A. Ciufo, M. L. Meyerson, B. K. Keitz and C. B. Mullins, *J. Mater. Chem. A*, 2019, **7**, 19396–19406.

52 J. Sienkiewicz-Gromiuk, I. Rusinek, Ł. Kurach and Z. Rzączyńska, *J Therm Anal Calorim*, 2016, **126**, 327–342.

53 J. F. Moulder, W. F. Stickle, P. E. Sobol and K. D. Bomben, *Handbook of X Ray Photoelectron Spectroscopy: A Reference Book of Standard Spectra for Identification and Interpretation of Xps Data*, Physical Electronics, Eden Prairie, Minn., Reissue., 1995.

54 A. S. Duke, E. A. Dolgopolova, R. P. Galhenage, S. C. Ammal, A. Heyden, M. D. Smith, D. A. Chen and N. B. Shustova, *J. Phys. Chem. C*, 2015, **119**, 27457–27466.

55 X. Li, H. Liu, X. Jia, G. Li, T. An and Y. Gao, *Science of The Total Environment*, 2018, **621**, 1533–1541.

56 W. Li, X. Wu, H. Liu, J. Chen, W. Tang and Y. Chen, *New J. Chem.*, 2015, **39**, 7060–7065.

57 W. Li, X. Wu, N. Han, J. Chen, X. Qian, Y. Deng, W. Tang and Y. Chen, *Sensors and Actuators B: Chemical*, 2016, **225**, 158–166.

58 N. Han, Y. Tian, X. Wu and Y. Chen, *Sensors and Actuators B: Chemical*, 2009, **138**, 228–235.

59 E. Borfecchia, S. Maurelli, D. Gianolio, E. Groppo, M. Chiesa, F. Bonino and C. Lamberti, *J. Phys. Chem. C*, 2012, **116**, 19839–19850.

60 N. Nijem, K. Fürsich, H. Bluhm, S. R. Leone and M. K. Gilles, *J. Phys. Chem. C*, 2015, **119**, 24781–24788.

61 C. Petit, B. Mendoza and T. J. Bandosz, *Langmuir*, 2010, **26**, 15302–15309.

62 N. C. Burtch, H. Jasuja and K. S. Walton, *Chem. Rev.*, 2014, **114**, 10575–10612.

63 F. Gul-E-Noor, B. Jee, A. Pöppl, M. Hartmann, D. Himsl and M. Bertmer, *Phys. Chem. Chem. Phys.*, 2011, **13**, 7783–7788.

64 J. B. Decoste, G. W. Peterson, M. W. Smith, C. A. Stone and C. R. Willis, *J. Am. Chem. Soc.*, 2012, **134**, 1486–1489.

65 Y. Sun, M. Ma, B. Tang, S. Li, L. Jiang, X. Sun, M. Que, C. Tao and Z. Wu, *Journal of Alloys and Compounds*, 2019, **808**, 151721.

66 Z. Lin, Z. Lv, X. Zhou, H. Xiao, J. Wu and Z. Li, *Ind. Eng. Chem. Res.*, 2018, **57**, 3765–3772.

67 H. Li, Z. Lin, X. Zhou, X. Wang, Y. Li, H. Wang and Z. Li, *Chemical Engineering Journal*, 2017, **307**, 537–543.